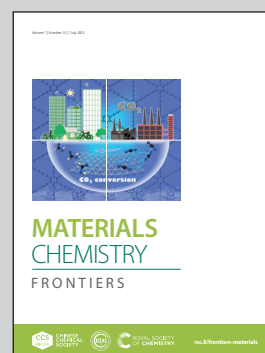


Highlighting the research activities of Professor Xiulin Yang's laboratory, School of Chemistry and Pharmaceutical Sciences, Guangxi Normal University, Guilin, China.

Electron-transfer enhancement of urchin-like  $\text{CoP-Ce}_2(\text{CO}_3)_2\text{O/NF}$  as an ultra-stable bifunctional catalyst for efficient overall water splitting

This work highlights the sea urchin-like heterojunction  $\text{CoP-Ce}_2(\text{CO}_3)_2\text{O}$  catalyst that shows superior performance and superb stability in electrocatalytic overall water splitting by modulating the electronic interaction at the interface.

As featured in:



See Tayirjan Taylor Isimjan and Xiulin Yang *et al.*, *Mater. Chem. Front.*, 2023, 7, 2628.

Registered charity number: 207890



CHINESE  
CHEMICAL  
SOCIETY



ROYAL SOCIETY  
OF CHEMISTRY

[rsc.li/frontiers-materials](https://rsc.li/frontiers-materials)

## RESEARCH ARTICLE

 View Article Online  
 View Journal | View Issue

 Cite this: *Mater. Chem. Front.*,  
 2023, 7, 2628

# Electron-transfer enhancement of urchin-like CoP–Ce<sub>2</sub>(CO<sub>3</sub>)<sub>2</sub>O/NF as an ultra-stable bifunctional catalyst for efficient overall water splitting†

 Lixia Wang,<sup>a</sup> Meilin Huang,<sup>a</sup> Mingcheng Gao,<sup>a</sup> Tayirjan Taylor Isimjan<sup>id</sup>\*<sup>b</sup> and Xiulin Yang<sup>id</sup>\*<sup>a</sup>

Effective control of strong electron interaction at heterogeneous interfaces is crucial for the creation of highly efficient and stable bifunctional catalysts for water splitting. In this work, we synthesized an urchin-like CoP–Ce<sub>2</sub>(CO<sub>3</sub>)<sub>2</sub>O catalyst on nickel foam (CoP–Ce<sub>2</sub>(CO<sub>3</sub>)<sub>2</sub>O/NF) via a facile hydrothermal and gas-phase phosphating process, which enhances active site exposure and improves catalytic reaction kinetics. Spectroscopy analysis reveals that the enhanced performance is due to the charge transfer between CoP and Ce<sub>2</sub>(CO<sub>3</sub>)<sub>2</sub>O and the unique urchin-like structure of the hybrid catalyst. The CoP–Ce<sub>2</sub>(CO<sub>3</sub>)<sub>2</sub>O/NF catalyst showed excellent hydrogen/oxygen evolution reaction (HER/OER) performance ( $\eta_{10} = 85.2$  and 205.5 mV) and robust long-term stability in 1.0 M KOH. Additionally, the CoP–Ce<sub>2</sub>(CO<sub>3</sub>)<sub>2</sub>O/NF<sup>(+)</sup>||CoP–Ce<sub>2</sub>(CO<sub>3</sub>)<sub>2</sub>O/NF<sup>(-)</sup> electrolyzer required only a low cell voltage of 1.82 V to produce 100 mA cm<sup>-2</sup> for overall water splitting, outperforming most previous catalysts. This work presents a strategy for interfacial engineering to improve the activity of bifunctional heterojunction electrocatalysts for overall water splitting.

 Received 6th February 2023,  
 Accepted 20th April 2023

DOI: 10.1039/d3qm00128h

[rsc.li/frontiers-materials](https://rsc.li/frontiers-materials)

## 1. Introduction

The depletion of fossil fuels has created a pressing need for the development of green and sustainable energy alternatives.<sup>1,2</sup> Contemporarily, hydrogen is considered as one of the most promising renewable and eco-friendly energy sources to replace fossil fuels, and alkaline water electrolysis is a key process for large-scale hydrogen production.<sup>3,4</sup> Water splitting is an encouraging energy storage and conversion technology involving cathodic hydrogen evolution reaction (HER) and anodic oxygen evolution reaction (OER).<sup>5</sup> Nevertheless, commercial catalysts are typically made with noble metals, which are expensive and scarce for extensive applications.<sup>6,7</sup> Consequently, exploring more efficient, cost-effective, and abundant non-precious metal-based catalysts with superior activity and stability is

necessary.<sup>8–10</sup> Various transition metal composites have been found to be promising candidates due to their low cost, abundant earth reserves and high electrocatalytic activity.<sup>11,12</sup> In particular, transition metal phosphides (TMPs) have significantly progressed in electrocatalysts.<sup>13</sup> The negative charge on P in TMPs restricts electron spread in the metal, leading to ionic and covalent bond coexistence in M–P, making TMPs more thermally and chemically stable.<sup>14</sup> This also narrows the energy gap between molecular orbitals, crucial for electrocatalysis.<sup>15</sup>

The utilization of CoP in catalysis is widespread due to its abundance, high electrical conductivity, and excellent catalytic activity and stability.<sup>16–18</sup> The moderate contact between phosphorus and reaction intermediates creates proton acceptor and hydride acceptor sites on the CoP surface.<sup>19,20</sup> Its combination of metal and semiconductor chemical bonds further enhances its intrinsic activity and stability.<sup>21,22</sup> However, due to the limited number of active sites, individual CoP typically displays poor electrochemical performance.<sup>23,24</sup> Researchers have therefore sought ways to optimize the catalyst morphology, regulate the active species' internal electronic structure, and construct heterostructures and interfaces to improve charge/electron transfer rates and increase active sites.<sup>25,26</sup> More attractively, due to the redox interaction between Ce<sup>3+</sup> and Ce<sup>4+</sup>, compounds of Ce usually have mixed electron/ion transport and improved catalytic properties.<sup>27–29</sup> Due to its unique electronic structure, Ce<sub>2</sub>(CO<sub>3</sub>)<sub>2</sub>O can activate

<sup>a</sup> Guangxi Key Laboratory of Low Carbon Energy Materials, School of Chemistry and Pharmaceutical Sciences, Guangxi Normal University, Guilin 541004, China. E-mail: xlyang@gxnu.edu.cn

<sup>b</sup> Saudi Arabia Basic Industries Corporation (SABIC) at King Abdullah University of Science and Technology (KAUST), Thuwal 23955-6900, Saudi Arabia. E-mail: isimjant@sabic.com

† Electronic supplementary information (ESI) available: Materials characterization, electrochemical measurements, ECSA calculations, XRD, SEM, XPS, electrocatalytic data and summary results. See DOI: <https://doi.org/10.1039/d3qm00128h>

water molecules in the electrolyte, resulting in excellent stability and corrosion resistance.<sup>30</sup> However, using  $\text{Ce}_2(\text{CO}_3)_2\text{O}$  alone may not be sufficient for high-efficiency water splitting. By combining  $\text{Ce}_2(\text{CO}_3)_2\text{O}$  with other materials, the synergistic effect can greatly enhance the electrocatalytic activity and improve its efficiency.<sup>31</sup> Heterostructure and interfacial engineering of CoP/Ce-based catalysts most probably further boosts catalytic activity by improving the charge/electron transfer rates and active site numbers.<sup>32–36</sup>

In this work, inspired by the unique electronic structure of Ce and the pervasive application of CoP in the field of catalysis, an urchin-like CoP– $\text{Ce}_2(\text{CO}_3)_2\text{O}/\text{NF}$  heterojunction catalyst was designed and constructed by a hydrothermal and gas-phase phosphating strategy. The optimized CoP– $\text{Ce}_2(\text{CO}_3)_2\text{O}/\text{NF}$  demonstrated exceptional HER/OER electrocatalytic performance ( $\eta_{10} = 85.2/205.5$  mV) and remarkable long-term durability in alkaline conditions, maintaining 400 and 280 h at  $10 \text{ mA cm}^{-2}$ , respectively. Meanwhile, the water-splitting electrolyzer device assembled by CoP– $\text{Ce}_2(\text{CO}_3)_2\text{O}/\text{NF}$  requires only 1.82 V to achieve  $100 \text{ mA cm}^{-2}$  and displayed excellent stability.

## 2. Experimental

### 2.1. Materials

All reagents were analytical grade and used without further purification. Cobalt(II) chloride ( $\text{CoCl}_2 \cdot 6\text{H}_2\text{O}$ ), cerium nitrate hexahydrate ( $\text{Ce}(\text{NO}_3)_3 \cdot 6\text{H}_2\text{O}$ , 99.95%), and ruthenium trichloride ( $\text{RuCl}_3 \cdot x\text{H}_2\text{O}$ , Ru: 37–40%) were obtained from Shanghai Aladdin Biochemical Technology Co., Ltd. Urea ( $\text{CO}(\text{NH}_2)_2$ ,  $\geq 99.0\%$ ), sodium hypophosphite monohydrate ( $\text{NaH}_2\text{PO}_2 \cdot \text{H}_2\text{O}$ , 99%), absolute ethanol ( $\text{C}_2\text{H}_5\text{OH}$ ,  $\geq 99.7\%$ ), Nafion (5% solution), and potassium hydroxide (KOH) were acquired from Guangxi Zoey Biotechnology Co., Ltd. Commercial Pt/C (20 wt% for platinum) was purchased from Alfa Aesar, and sulphuric acid ( $\text{H}_2\text{SO}_4$ , 95.0–98.0%) was provided by Xilong Chemical Co., Ltd. The nickel foam (NF) used as a substrate was obtained from Suzhou Sinero Technology Co., Ltd ( $3 \text{ cm} \times 1.5 \text{ cm}$ ).

### 2.2. Synthesis of Co–Ce species on NF

The NF was ultrasonically cleaned with 0.5 M  $\text{H}_2\text{SO}_4$ , deionized water and ethanol for 15 min to remove impurities. A solution of 1.5 mmol ( $\text{CoCl}_2 \cdot 6\text{H}_2\text{O}$ ), 0.5 mmol  $\text{Ce}(\text{NO}_3)_3 \cdot 6\text{H}_2\text{O}$ , and 2 mmol urea in 40 mL deionized (DI) water was prepared and transferred to a 100 mL Teflon-line stainless steel autoclave. The pretreated NF was then placed in the autoclave, and heated to  $150^\circ\text{C}$  for 8 h. After cooling to room temperature naturally, the product was washed with DI water and dried at room temperature. To study the effect of Co/Ce ratio on the composite material, five materials were synthesized with a total of 2 mmol  $\text{Co}^{2+}$  and  $\text{Ce}^{3+}$  and varying molar ratios of Co/Ce (4/0, 3/1, 2/2, 1/3, and 0/4).

### 2.3. Synthesis of CoP– $\text{Ce}_2(\text{CO}_3)_2\text{O}/\text{NF}$

Two  $1 \text{ cm} \times 1.5 \text{ cm}$  pieces of Co–Ce species and 1.0 g of  $\text{NaH}_2\text{PO}_2 \cdot \text{H}_2\text{O}$  were placed in the middle and upstream of a quartz tube, respectively. Subsequently, the tube furnace was heated to  $350^\circ\text{C}$  in a  $\text{N}_2$  atmosphere for 2 h. The resulting

products were rinsed with DI water and dried at room temperature. CoP– $\text{Ce}_2(\text{CO}_3)_2\text{O}/\text{NF}$  refers to samples obtained with a Co/Ce of 3/1 unless stated otherwise. To make CoP/NF or  $\text{Ce}_2(\text{CO}_3)_2\text{O}/\text{NF}$ , the process was the same as CoP– $\text{Ce}_2(\text{CO}_3)_2\text{O}/\text{NF}$ , but without the respective Co or Ce source.

### 2.4. Preparation of $\text{RuO}_2/\text{NF}$ and Pt/C/NF

The  $\text{RuO}_2$  powder was made by heating  $\text{RuCl}_3$  in air at  $400^\circ\text{C}$ . Afterwards, 2 mg of  $\text{RuO}_2$  or Pt/C was mixed with 200  $\mu\text{L}$  of DI water, 200  $\mu\text{L}$  of ethanol and 5  $\mu\text{L}$  of 5% Nafion, creating a homogeneous ink through ultrasonic dispersion. The ink was drop-cast on the NF surface ( $1 \text{ cm} \times 1.5 \text{ cm}$ ) and dried in air.

## 3. Results and discussion

### 3.1. Structural and morphological characterizations

The synthesis of CoP– $\text{Ce}_2(\text{CO}_3)_2\text{O}/\text{NF}$  is illustrated in Fig. 1a. A facile hydrothermal reaction is used to create Co–Ce species/NF, followed by gas-phase phosphating treatment at  $350^\circ\text{C}$  to convert it to CoP– $\text{Ce}_2(\text{CO}_3)_2\text{O}/\text{NF}$ . The X-ray diffraction (XRD) patterns provided in Fig. S2 (ESI<sup>†</sup>) confirm that the strong peaks of Co-species/NF match the signals of  $\text{Co}(\text{CO}_3)_0.5(\text{OH}) \cdot 0.11\text{H}_2\text{O}$  (JCPDS: 48-0083). The diffraction peaks of CoP/NF obtained after phosphorylation of Co-species/NF are in accordance with the characteristic signal of CoP (JCPDS: 29-0497) in Fig. 1b.<sup>37</sup> Surprisingly, the diffraction peaks of Ce-species/NF before and after phosphorylation were consistent, as evidenced by the standard pattern of  $\text{Ce}_2(\text{CO}_3)_2\text{O} \cdot \text{H}_2\text{O}$  (JCPDS: 44-0617), although there were some differences in the intensity of the peaks (Fig. 1c). This indicates that selective phosphorylation of the Co–Ce species has occurred.<sup>38</sup> The XRD pattern of the Co–Ce precursor after phosphatizing shows that the diffraction peaks are in accordance with the standard patterns of CoP (JCPDS: 29-0497) and  $\text{Ce}_2(\text{CO}_3)_2\text{O} \cdot \text{H}_2\text{O}$  (JCPDS: 44-0617); hence, the obtained sample is denominated as CoP– $\text{Ce}_2(\text{CO}_3)_2\text{O}/\text{NF}$  for convenience (Fig. 1d).

Scanning electron microscopy (SEM) was used to investigate morphological evolution in materials with varying Co/Ce ratios. The precursor form changed from cross-linked nanowires (with only Co) to nanorods with increasing Ce ratio (Fig. S3, ESI<sup>†</sup>). The phosphorylation process did not alter the structure (Fig. S4, ESI<sup>†</sup>). The urchin-like CoP– $\text{Ce}_2(\text{CO}_3)_2\text{O}/\text{NF}$  is more beneficial in exposing abundant active sites and improving the electrocatalytic activity (Fig. 2a). Meanwhile, the transmission electron microscopy (TEM) image showed that the CoP– $\text{Ce}_2(\text{CO}_3)_2\text{O}/\text{NF}$  consists of nanowires with smooth surfaces, likely due to the higher Co content (Fig. 2b). According to Fig. 2c, the high resolution TEM (HR-TEM) image displayed that the interplanar spacing of CoP– $\text{Ce}_2(\text{CO}_3)_2\text{O}/\text{NF}$  was 0.270 and 0.199 nm, corresponding to the (311) and (112) of  $\text{Ce}_2(\text{CO}_3)_2\text{O} \cdot \text{H}_2\text{O}$  and CoP, respectively. The selective area electron diffraction (SAED) pattern further confirmed the XRD results, identifying the diffraction rings as the (301) and (111) planes of CoP, and (200) planes of  $\text{Ce}_2(\text{CO}_3)_2\text{O} \cdot \text{H}_2\text{O}$  (Fig. 2d). The energy dispersive X-ray spectroscopy (EDS) results confirmed the presence of Co,

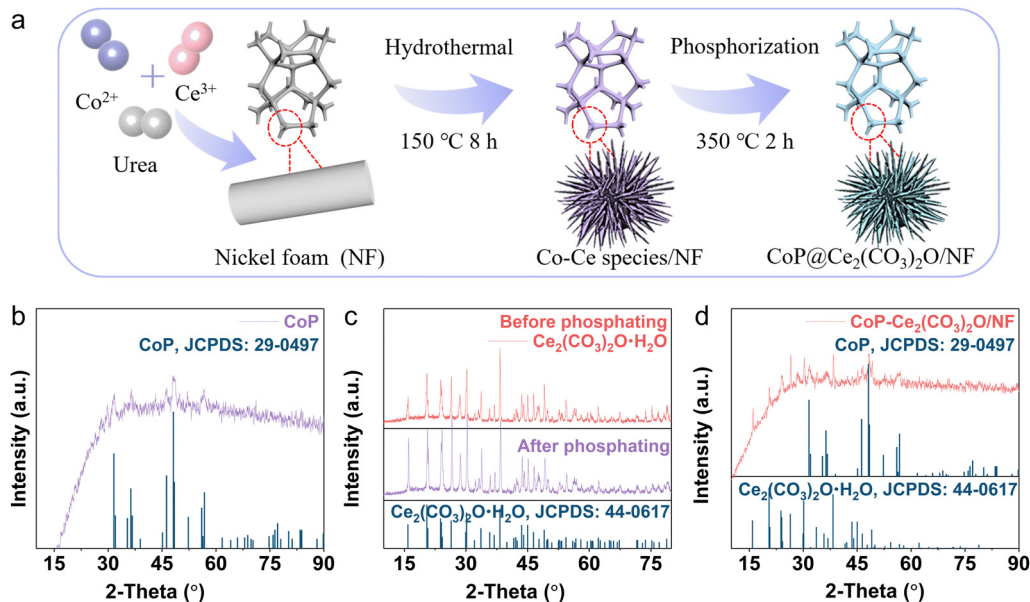


Fig. 1 (a) Schematic diagram for the synthesis of CoP– $\text{Ce}_2(\text{CO}_3)_2\text{O}/\text{NF}$ . (b) XRD pattern of CoP/NF. (c) XRD patterns of Ce-species/NF, and (d) Ce–Co species/NF before and after phosphating.

Ce, P and O elements (Fig. 2e) with uniform distribution throughout the CoP– $\text{Ce}_2(\text{CO}_3)_2\text{O}/\text{NF}$ , as shown in the high-angle annular dark-field scanning TEM (HAADF) image and elemental mapping (Fig. 2f).

X-ray photoelectron spectroscopy (XPS) was conducted to analyze the valence state and chemical composition of CoP– $\text{Ce}_2(\text{CO}_3)_2\text{O}/\text{NF}$ . The full survey spectrum showed the presence of Co, Ce, O and P elements, confirming the TEM results (Fig. S5a, ESI<sup>†</sup>). The high-resolution C 1s spectrum demonstrated four peaks with binding energies of 284.0, 284.8, 286.0, and

288.0 eV, corresponding to C=C, C–C, C–O, and C=O, respectively (Fig. S5b, ESI<sup>†</sup>).<sup>39</sup> As shown in Fig. 3a, the Co 2p<sub>3/2</sub> spectrum of the CoP– $\text{Ce}_2(\text{CO}_3)_2\text{O}/\text{NF}$  is divided into four peaks with binding energies of 778.3, 781.3, 783.2 and 785.3 eV, corresponding to the Co–P, Co(II)–O, Co(III)–O and satellite peaks, respectively.<sup>40</sup> It is worth mentioning that the Co 2p peak of CoP– $\text{Ce}_2(\text{CO}_3)_2\text{O}/\text{NF}$  is shifted negatively by approximately 0.3 eV compared to CoP/NF, indicating that  $\text{Ce}_2(\text{CO}_3)_2\text{O}$  acts as an electron donor. Furthermore, the high-resolution Ce 3d<sub>5/2</sub> spectrum (Fig. 3b) shows that the peak of CoP– $\text{Ce}_2(\text{CO}_3)_2\text{O}/\text{NF}$  is convoluted into two peaks for Ce<sup>4+</sup> (881.8 eV) and Ce<sup>3+</sup> (885.6 eV),<sup>39,41</sup> which are positively shifted by 0.4 eV compared to  $\text{Ce}_2(\text{CO}_3)_2\text{O}/\text{NF}$ , suggesting that Co acts as an electron acceptor. The high-resolution O 1s region (Fig. 3c) consists of three components at 530.1, 531.4, and 532.3 eV, attributed to metallic oxygen (M–O), OH<sup>–</sup>, and surface adsorbed water (H<sub>2</sub>O<sub>ads</sub>), respectively.<sup>42</sup> For the P 2p spectrum, the apparent peak at 133.7 eV reflects the presence of P–O species, arising from superficial oxidation.<sup>11</sup> Additionally, the peaks at 128.7 and 130.1 eV are ascribed to the Co–P bonds of CoP/NF and CoP– $\text{Ce}_2(\text{CO}_3)_2\text{O}/\text{NF}$ .<sup>37</sup> These results confirm that there is an electron transfer between CoP/NF and  $\text{Ce}_2(\text{CO}_3)_2\text{O}/\text{NF}$ , which contributes to the strong electronic coupling between them, thereby promoting the electrocatalytic performance.<sup>43</sup>

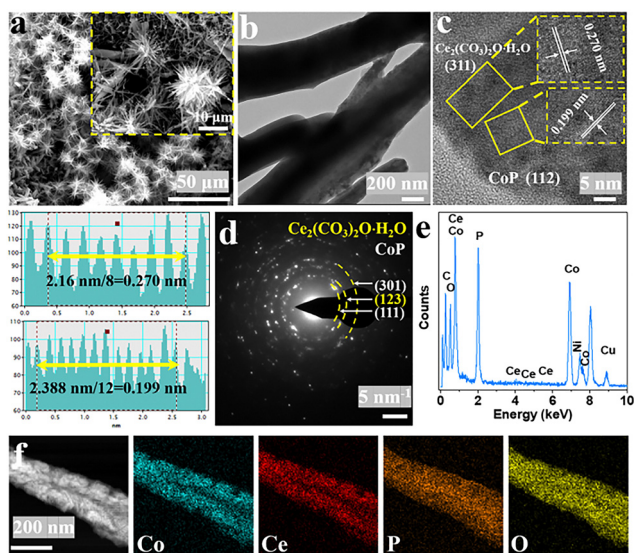


Fig. 2 (a) SEM image with (inset) the high-magnification SEM image, (b) TEM image, (c) HR-TEM image, (d) SAED image, (e) EDS spectrum profile, and (f) HAADF-STEM image and corresponding element mappings of CoP– $\text{Ce}_2(\text{CO}_3)_2\text{O}/\text{NF}$ .

### 3.2. Electrocatalytic performance

To evaluate the electrocatalytic performance of the catalysts, linear sweep voltammetry (LSV) in 1.0 M KOH was used to obtain polarization curves. The activity of samples made with different hydrothermal times (6, 8, and 10 h) was evaluated, with 8 h showing the best HER and OER activity (Fig. S6 and S7, ESI<sup>†</sup>). Furthermore, the activity and stability of the catalyst were found to be poor when using only Co, Ce, or Co/Ce ratios of 1 : 3

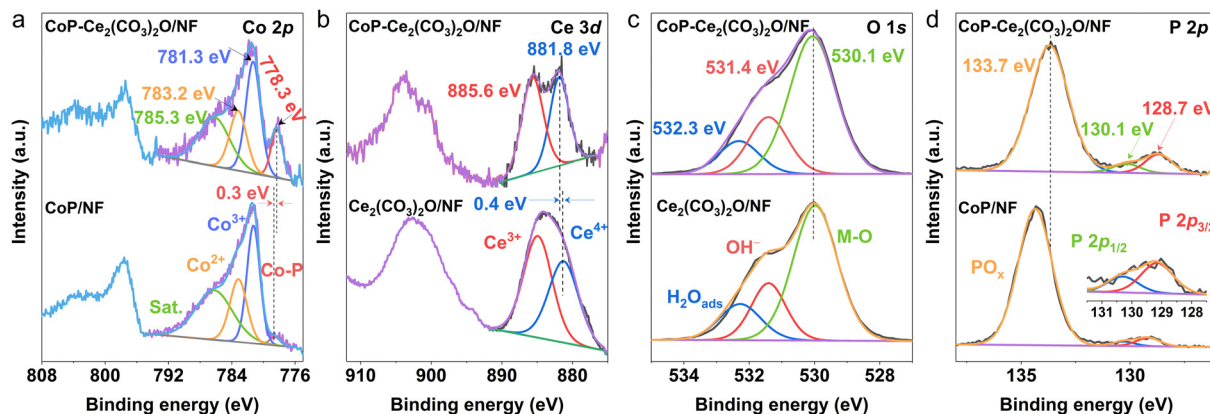


Fig. 3 High-resolution XPS spectra of (a) Co 2p, (b) Ce 3d, (c) O 1s, and (d) P 2p regions in CoP–Ce<sub>2</sub>(CO<sub>3</sub>)<sub>2</sub>O/NF, CoP/NF, and Ce<sub>2</sub>(CO<sub>3</sub>)<sub>2</sub>O/NF, respectively.

or 2 : 2, as shown in Fig. S8 and S9 (ESI<sup>†</sup>). However, the catalysts with a Co/Ce ratio of 3/1 exhibited the best performance. Additionally, we conducted stability tests on the as-prepared electrocatalysts with different Co/Ce ratios by subjecting them to a constant current of 10 mA cm<sup>-2</sup> (Fig. S10, ESI<sup>†</sup>). The results suggest that the incorporation of Ce species can enhance the stability of CoP. Therefore, the Co and Ce content are crucial factors that affect the electrocatalytic activity and stability of the catalyst. The HER activities of the samples are illustrated in Fig. 4a. CoP–Ce<sub>2</sub>(CO<sub>3</sub>)<sub>2</sub>O/NF presents a lower potential of 85.2 mV at 10 mA cm<sup>-2</sup>, compared to Pt/C/NF, and much lower than CoP/NF (206.3 mV) and Ce<sub>2</sub>(CO<sub>3</sub>)<sub>2</sub>O/NF (211.8 mV), making it superior to most recently reported HER catalysts (Fig. 4b and Table S2, ESI<sup>†</sup>). Additionally, compared to CoP/NF (113.4 mV dec<sup>-1</sup>) and Ce<sub>2</sub>(CO<sub>3</sub>)<sub>2</sub>O/NF (120.7 mV dec<sup>-1</sup>), CoP–Ce<sub>2</sub>(CO<sub>3</sub>)<sub>2</sub>O/NF displayed a lower Tafel slope of 65.2 mV dec<sup>-1</sup> (Fig. 4c), indicating that the Heyrovsky step (H<sup>+</sup> + H<sub>2</sub>O + e<sup>-</sup> → H<sub>2</sub> + OH<sup>-</sup>) was the rate-limiting step.<sup>44</sup> Electrochemical impedance spectroscopy (EIS) was employed to assess the charge-transfer kinetics. The charge

transfer resistance ( $R_{ct}$ ) of CoP–Ce<sub>2</sub>(CO<sub>3</sub>)<sub>2</sub>O/NF was substantially lower than that of the other comparison samples, demonstrating the fastest charge transfer kinetics (Fig. 4d).<sup>45</sup> Furthermore, the electrochemical double layer capacitance ( $C_{dl}$ ) was derived from the collected CV curves at different scan rates (Fig. S11–S13, ESI<sup>†</sup>), and the electrochemically active surface area (ECSA) was calculated from the  $C_{dl}$  measurements to reveal the intrinsic activity of the catalyst.<sup>46</sup> CoP–Ce<sub>2</sub>(CO<sub>3</sub>)<sub>2</sub>O/NF has an immense  $C_{dl}$  value (37.0 mF cm<sup>-2</sup>), which is more significant than CoP/NF (10.9 mF cm<sup>-2</sup>) and Ce<sub>2</sub>(CO<sub>3</sub>)<sub>2</sub>O/NF (11.3 mF cm<sup>-2</sup>) in Fig. 4e, implying that the larger ECSA has more available active sites (Fig. S14, ESI<sup>†</sup>).<sup>44</sup> As depicted in Fig. 4f, CoP–Ce<sub>2</sub>(CO<sub>3</sub>)<sub>2</sub>O/NF exhibited negligible potential change at 10 mA cm<sup>-2</sup> after 400 h, signifying its robust HER stability.

The OER catalytic activity of all samples and RuO<sub>2</sub>/NF was further investigated. As presented in Fig. 5a, CoP–Ce<sub>2</sub>(CO<sub>3</sub>)<sub>2</sub>O/NF only requires an overpotential of 205.5 mV at a current density of 10 mA cm<sup>-2</sup>, much lower than CoP/NF (251.5 mV)

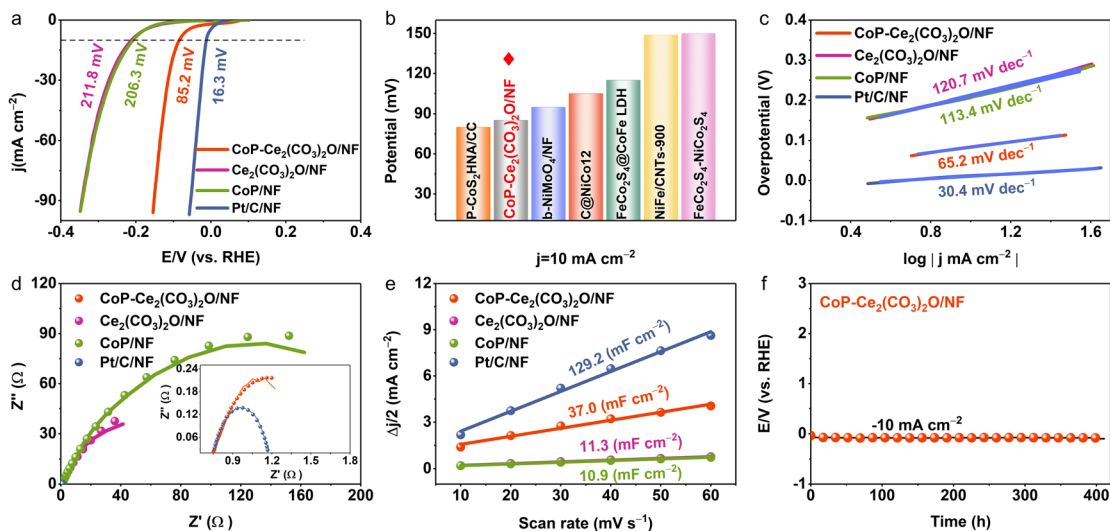


Fig. 4 HER performance of different catalysts and Pt/C/NF in 1.0 M KOH. (a) LSV polarization curves, (b) comparison with the potentials of recently reported catalysts for HER activity at 10 mA cm<sup>-2</sup>, (c) corresponding Tafel slopes, (d) electrochemical impedance spectroscopy (EIS), (e) double layer capacitance ( $C_{dl}$ ), and (f) stability of the CoP–Ce<sub>2</sub>(CO<sub>3</sub>)<sub>2</sub>O/NF catalyst for the HER.

and  $\text{Ce}_2(\text{CO}_3)_2\text{O}/\text{NF}$  (227.8 mV), and slightly higher than  $\text{RuO}_2/\text{NF}$  (185.1 mV). The Tafel slope was employed to evaluate the catalytic reaction kinetics of the OER, where the Tafel slope of  $\text{CoP}-\text{Ce}_2(\text{CO}_3)_2\text{O}/\text{NF}$  is  $75.6 \text{ mV dec}^{-1}$ , close to that of commercial  $\text{RuO}_2/\text{NF}$  ( $51.9 \text{ mV dec}^{-1}$ ), but lower than that of  $\text{Ce}_2(\text{CO}_3)_2\text{O}/\text{NF}$  ( $93.7 \text{ mV dec}^{-1}$ ) and  $\text{CoP}/\text{NF}$  ( $92.8 \text{ mV dec}^{-1}$ ), demonstrating fast kinetics (Fig. 5b).<sup>47</sup> In contrast, the overpotentials and Tafel slopes of various catalysts at current densities of 10 and  $100 \text{ mA cm}^{-2}$  are summarized in Fig. 5c, indicating that the OER performance of  $\text{CoP}-\text{Ce}_2(\text{CO}_3)_2\text{O}/\text{NF}$  exceeds those of single comparison samples. To evaluate the intrinsic catalytic activity of the catalysts, we utilized the TOF (turnover frequency) values derived from the ICP results (Table S1, ESI<sup>†</sup>).<sup>48</sup> We plotted the TOF values of the catalysts under gradually increasing applied voltages in Fig. S15 (ESI<sup>†</sup>). Notably,  $\text{CoP}-\text{Ce}_2(\text{CO}_3)_2\text{O}/\text{NF}$  displayed the highest TOF value, which is a clear indication of its exceptional intrinsic activity. As indicated in Fig. 5d and Table S3 (ESI<sup>†</sup>), the  $\text{CoP}-\text{Ce}_2(\text{CO}_3)_2\text{O}/\text{NF}$  has advantages over the latest reported OER catalysts. Furthermore, the  $\text{CoP}-\text{Ce}_2(\text{CO}_3)_2\text{O}/\text{NF}$  also has a smaller  $R_{ct}$  than other catalysts, demonstrating the enhanced charge transfer performance through the  $\text{CoP}/\text{Ce}_2(\text{CO}_3)_2\text{O}$  interface (Fig. 5e).<sup>47</sup> In addition, the performance exhibits negligible degradation after approximately 280 h of continuous operation at  $10 \text{ mA cm}^{-2}$  (Fig. 5f), further confirming its high OER stability.

Considering the excellent HER and OER performance of  $\text{CoP}-\text{Ce}_2(\text{CO}_3)_2\text{O}/\text{NF}$ , a bifunctional electrode device using  $\text{CoP}-\text{Ce}_2(\text{CO}_3)_2\text{O}/\text{NF}$  as the anode and cathode was constructed to evaluate the bifunctional catalytic performance in overall water splitting (Fig. 6a). As seen in Fig. 6b,  $\text{CoP}-\text{Ce}_2(\text{CO}_3)_2\text{O}/\text{NF}^{(+)}||\text{CoP}-\text{Ce}_2(\text{CO}_3)_2\text{O}/\text{NF}^{(-)}$  exhibits a cell voltage of 1.82 V at  $100 \text{ mA cm}^{-2}$ , slightly lower than the commercial  $\text{RuO}_2/\text{NF}^{(+)}||\text{Pt}/\text{C}/\text{NF}^{(-)}$  (1.73 V). It is noteworthy that the situation is reversed at high current density ( $>400 \text{ mA cm}^{-2}$ ), and the

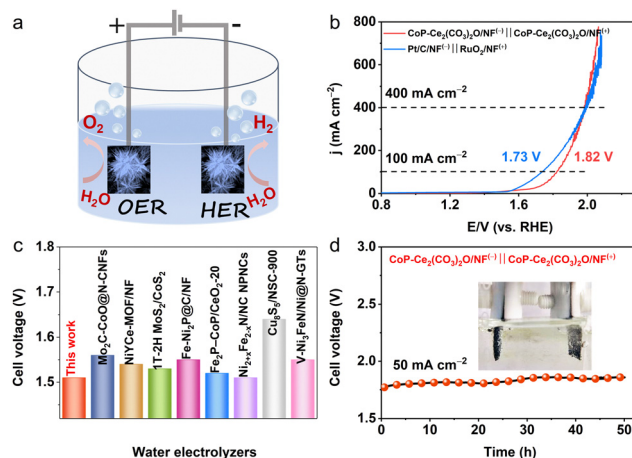


Fig. 6 (a) Schematic diagram of the overall water splitting electrolyzer using  $\text{CoP}-\text{Ce}_2(\text{CO}_3)_2\text{O}/\text{NF}$  as a bifunctional catalyst. (b) Comparison of the polarization curves of  $\text{CoP}-\text{Ce}_2(\text{CO}_3)_2\text{O}/\text{NF}^{(+)}||\text{CoP}-\text{Ce}_2(\text{CO}_3)_2\text{O}/\text{NF}^{(-)}$  and the  $\text{RuO}_2/\text{NF}^{(+)}||\text{Pt}/\text{C}/\text{NF}^{(-)}$  at high currents in 1.0 M KOH. (c) Comparing cell voltages with the recently reported electrolyzers at  $10 \text{ mA cm}^{-2}$  in 1.0 M KOH. (d) Long-term stability test of  $\text{CoP}-\text{Ce}_2(\text{CO}_3)_2\text{O}/\text{NF}^{(+)}||\text{CoP}-\text{Ce}_2(\text{CO}_3)_2\text{O}/\text{NF}^{(-)}$  at  $50 \text{ mA cm}^{-2}$  in 1.0 M KOH.

bifunctional  $\text{CoP}-\text{Ce}_2(\text{CO}_3)_2\text{O}/\text{NF}^{(+/-)}$  shows better catalytic performance. Moreover, the designed bifunctional catalyst outperformed most previously reported bifunctional catalysts at  $10 \text{ mA cm}^{-2}$  (Fig. 6c and Table S4, ESI<sup>†</sup>). Furthermore, the chronopotentiometry curve of  $\text{CoP}-\text{Ce}_2(\text{CO}_3)_2\text{O}/\text{NF}^{(+)}||\text{CoP}-\text{Ce}_2(\text{CO}_3)_2\text{O}/\text{NF}^{(-)}$  at  $50 \text{ mA cm}^{-2}$  was maintained for 50 h (Fig. 6d), confirming the high durability for water splitting.

To investigate the composition changes of  $\text{CoP}-\text{Ce}_2(\text{CO}_3)_2\text{O}/\text{NF}$  after prolonged OER stability testing, we conducted a series of characterizations. SEM images revealed a slight collapse in the morphology of the catalyst after OER stability testing, while the morphology became rough only after the HER (Fig. S15, ESI<sup>†</sup>).

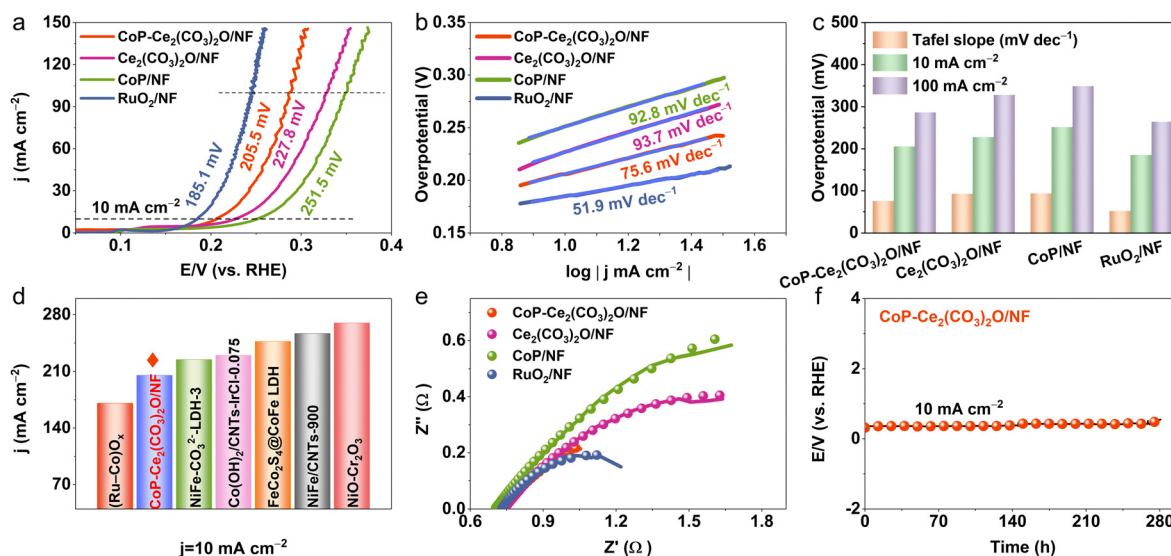


Fig. 5 OER performance of different catalysts and  $\text{RuO}_2/\text{CC}$  in 1.0 M KOH. (a) LSV polarization curves, (b) corresponding Tafel slopes, (c) summary of overpotentials (at 10 and  $200 \text{ mA cm}^{-2}$ ) and Tafel plots, (d) comparison with the overpotentials of recently reported catalysts for OER activity at  $10 \text{ mA cm}^{-2}$ , (e) electrochemical impedance spectroscopy (EIS), and (f) stability of the  $\text{CoP}-\text{Ce}_2(\text{CO}_3)_2\text{O}/\text{NF}$  catalyst for the OER.

XRD results showed that the substance after OER stability testing was consistent with  $\text{Co}_3\text{O}_4$  (JCPDS: 09-0418) and  $\text{CeO}_2$  (JCPDS: 01-0800), indicating the formation of the corresponding oxides on the catalyst's surface (Fig. S16, ESI<sup>†</sup>). Furthermore, XPS analysis demonstrated an increase in the ratio of  $\text{Co}^{3+}$  and  $\text{M-O}$  after stability testing (Fig. S17, ESI<sup>†</sup>), implying the presence of more oxygen-containing species and phosphides on the catalyst surface.<sup>49</sup> Based on our findings, we have determined that the CoP was indeed oxidized during the OER process. Therefore, we now believe that the primary benefit of the phosphatization process is the generation of a distinctive morphology that facilitates better mass transfer. The advantage cannot be achieved with oxides alone.

### 3.3. Catalytic mechanism analysis

Based on the above discussion, the augmenting performance and robust stability of  $\text{CoP-Ce}_2(\text{CO}_3)_2\text{O/NF}$  for the HER/OER are attributed to the heterojunction and the strong synergistic effect at the interface of CoP and  $\text{Ce}_2(\text{CO}_3)_2\text{O}$ . The XPS results confirmed the electronic interaction between CoP and  $\text{Ce}_2(\text{CO}_3)_2\text{O}$ , indicating that electrons were transferred from  $\text{Ce}_2(\text{CO}_3)_2\text{O}$  to CoP species.<sup>50</sup> Therefore, the presence of  $\text{Ce}_2(\text{CO}_3)_2\text{O}$  makes the Co component in CoP more positively charged, while P is negatively charged. In the alkaline medium of the HER, the acidic Co nodes ( $\delta^+$ ) can much more easily absorb  $\text{H}_2\text{O}$  molecules. An electron is obtained by the closely neighboring basic P center ( $\delta^-$ ) as the proton-acceptor center splits a  $\text{H}_2\text{O}$  molecule to form adsorbed  $\text{H}^*$  ( $\text{M} + \text{e}^- + \text{H}_2\text{O} \rightarrow \text{M-H}^* + \text{OH}^-$ ).<sup>51</sup> Then, the adsorbed  $\text{H}^*$  further combines with an electron and another  $\text{H}_2\text{O}$  molecule, and simultaneously releases an  $\text{H}_2$  molecule *via* the Heyrovsky mechanism ( $\text{M-H}^* + \text{H}_2\text{O} + \text{e}^- \rightarrow \text{M} + \text{OH}^- + \text{H}_2$ ).<sup>52</sup> During the OER process, the CoP surface in the  $\text{CoP-Ce}_2(\text{CO}_3)_2\text{O}$  heterostructure is first oxidized into a thin layer of cobalt oxide or oxyhydroxide.<sup>50,52</sup> Due to the lower work function of  $\text{Co}_3\text{O}_4$  (4.5 eV) compared to  $\text{CeO}_2$  (4.75 eV), electrons are partially transferred from  $\text{Co}_3\text{O}_4$  to  $\text{CeO}_2$ . This results in the formation of electron-deficient Co oxide and electron-rich  $\text{CeO}_2$ .<sup>53,54</sup> Therefore, the electron-deficient Co site can more easily adsorb a hydroxyl ( $\text{OH}^- + * \rightarrow \text{OH}_{\text{ads}} + \text{e}^-$ ), and donates a proton subsequently ( $\text{OH}_{\text{ads}} + \text{OH}^- \rightarrow \text{O}_{\text{ads}} + \text{H}_2\text{O} + \text{e}^-$ ). Then  $\text{O}^*$  is attacked by another  $\text{OH}^-$  and deprotonated to form  $^*\text{OOH}$  ( $\text{OOH}_{\text{ads}} + \text{OH}^- \rightarrow \text{O}_{2\text{ads}} + \text{H}_2\text{O} + \text{e}^-$ ). Finally, the proton-coupled electrons transfer and release  $\text{O}_2$  ( $\text{O}_{2\text{ads}} = \text{O}_2 + *$ ).<sup>48</sup> The role of  $\text{Ce}_2(\text{CO}_3)_2\text{O}$  is not negligible, which provides high conductivity and regulates the binding energy of the intermediates.<sup>55</sup> Besides, the urchin-like morphology facilitates electrolyte transport/gas diffusion,<sup>56</sup> and the  $\text{CoP/Ce}_2(\text{CO}_3)_2\text{O}$  heterogeneous interface provides abundant electrochemically active sites and promotes charge transfer, thus improving the catalytic performance.<sup>57,58</sup>

## 4. Conclusions

In summary, an urchin-like  $\text{CoP-Ce}_2(\text{CO}_3)_2\text{O/NF}$  was constructed by a facile hydrothermal and selective phosphating process. Benefiting from the electron transfer effect between CoP and  $\text{Ce}_2(\text{CO}_3)_2\text{O}$  species, as well as the urchin-like structure

supports for more active sites, the electrocatalytic performance and reaction kinetics of  $\text{CoP-Ce}_2(\text{CO}_3)_2\text{O/NF}$  are significantly improved and show impressive long-term durability. Consequently, the  $\text{CoP-Ce}_2(\text{CO}_3)_2\text{O/NF}$  exhibits low potentials of 85.2 and 205.5 mV to deliver  $10 \text{ mA cm}^{-2}$  for the HER and OER, respectively. More remarkably, the  $\text{CoP-Ce}_2(\text{CO}_3)_2\text{O/NF}^{(+)||\text{CoP-Ce}_2(\text{CO}_3)_2\text{O/NF}^{(-)}$  electrolyzer achieves  $100 \text{ mA cm}^{-2}$  at a low cell voltage of 1.82 V for overall water splitting. This work sheds light on the implications of the interfacial electron transfer effects and serves as a strategy for designing highly efficient electrocatalysts for overall water splitting.

## Author contributions

Lixia Wang: investigation, methodology, writing – original draft. Meilin Huang: investigation, data curation. Mingcheng Gao: data curation. Tayirjan Taylor Isimjan: writing – review & editing. Xiulin Yang: supervision, writing – review & editing.

## Conflicts of interest

There are no conflicts to declare.

## Acknowledgements

This work has been supported by the National Natural Science Foundation of China (no. 21965005), Natural Science Foundation of Guangxi Province (2021GXNSFAA076001), Project of High-Level Talents of Guangxi (F-KA18015), and Guangxi Technology Base and Talent Subject (GUIKE AD18126001, GUIKE AD20297039).

## Notes and references

- 1 C. Chen, H. Tian, Z. Fu, X. Cui, F. Kong, G. Meng, Y. Chen, F. Qi, Z. Chang, L. Zhu, H. Huang, B. Y. Xia and J. Shi, Pt NPs-loaded siloxene nanosheets for hydrogen co-evolutions from  $\text{Zn-H}_2\text{O}$  fuel cells-powered water-splitting, *Appl. Catal., B*, 2022, **304**, 121008.
- 2 C. Zhang, Y. Xue, L. Hui, Y. Fang, Y. Liu and Y. Li, Graphdiyne@ $\text{NiO}_x(\text{OH})_y$  heterostructure for efficient overall water splitting, *Mater. Chem. Front.*, 2021, **5**, 5305–5311.
- 3 X. Ding, J. Yu, W. Huang, D. Chen, W. Lin and Z. Xie, Modulation of the interfacial charge density on  $\text{Fe}_2\text{P-CoP}$  by coupling  $\text{CeO}_2$  for accelerating alkaline electrocatalytic hydrogen evolution reaction and overall water splitting, *Chem. Eng. J.*, 2023, **451**, 138550.
- 4 J.-W. Zhao, H. Zhang, C.-F. Li, X. Zhou, J.-Q. Wu, F. Zeng, J. Zhang and G.-R. Li, Key roles of surface Fe sites and Sr vacancies in the perovskite for an efficient oxygen evolution reaction via lattice oxygen oxidation, *Energy Environ. Sci.*, 2022, **15**, 3912–3922.
- 5 X. Wang, H. Huang, J. Qian, Y. Li and K. Shen, Intensified Kirkendall Effect Assisted Construction of Double-Shell

- Hollow Cu-Doped CoP Nanoparticles Anchored by Carbon Arrays for Water Splitting, *Appl. Catal., B*, 2022, **325**, 122295.
- 6 P. Mukherjee, K. Sathiyam, R. S. Vishwanath and T. Zidki, Anchoring MoS<sub>2</sub> on an ethanol-etched Prussian blue analog for enhanced electrocatalytic efficiency for the oxygen evolution reaction, *Mater. Chem. Front.*, 2022, **6**, 1770–1778.
  - 7 J.-W. Zhao, C.-F. Li, Z.-X. Shi, J.-L. Guan and G.-R. Li, Boosting Lattice Oxygen Oxidation of Perovskite to Efficiently Catalyze Oxygen Evolution Reaction by FeOOH Decoration, *Research*, 2020, **2020**, 6961578.
  - 8 N. Yao, T. Tan, F. Yang, G. Cheng and W. Luo, Well-aligned metal-organic framework array-derived CoS<sub>2</sub> nanosheets toward robust electrochemical water splitting, *Mater. Chem. Front.*, 2018, **2**, 1732–1738.
  - 9 C.-F. Li, L.-J. Xie, J.-W. Zhao, L.-F. Gu, H.-B. Tang, L. Zheng and G.-R. Li, Interfacial Fe–O–Ni–O–Fe Bonding Regulates the Active Ni Sites of Ni-MOFs via Iron Doping and Decorating with FeOOH for Super-Efficient Oxygen Evolution, *Angew. Chem., Int. Ed.*, 2022, **61**, e202116934.
  - 10 C.-F. Li, L.-J. Xie, J.-W. Zhao, L.-F. Gu, J.-Q. Wu and G.-R. Li, Interfacial electronic modulation by Fe<sub>2</sub>O<sub>3</sub>/NiFe-LDHs heterostructures for efficient oxygen evolution at high current density, *Appl. Catal., B*, 2022, **306**, 121097.
  - 11 Y. Wang, Y. Jiao, H. Yan, G. Yang, C. Tian, A. Wu, Y. Liu and H. Fu, Vanadium-Incorporated CoP<sub>2</sub> with Lattice Expansion for Highly Efficient Acidic Overall Water Splitting, *Angew. Chem., Int. Ed.*, 2022, **61**, e202116233.
  - 12 C.-F. Li, T.-Y. Shuai, L.-R. Zheng, H.-B. Tang, J.-W. Zhao and G.-R. Li, The key role of carboxylate ligands in Ru@Ni-MOFs/NF in promoting water dissociation kinetics for effective hydrogen evolution in alkaline media, *Chem. Eng. J.*, 2023, **451**, 138618.
  - 13 H. Yang, P. Guo, R. Wang, Z. Chen, H. Xu, H. Pan, D. Sun, F. Fang and R. Wu, Sequential Phase Conversion-Induced Phosphides Heteronanorod Arrays for Superior Hydrogen Evolution Performance to Pt in Wide pH Media, *Adv. Mater.*, 2022, **20**, e2107548.
  - 14 Q. Ma, H. Jin, F. Xia, H. Xu, J. Zhu, R. Qin, H. Bai, B. Shuai, W. Huang, D. Chen, Z. Li, J. Wu, J. Yu and S. Mu, Ultralow Ru-assisted and vanadium-doped flower-like CoP/Ni<sub>2</sub>P heterostructure for efficient water splitting in alkali and seawater, *J. Mater. Chem. A*, 2021, **9**, 26852–26860.
  - 15 J. Li, Y. Kang, Z. Lei and P. Liu, Well-controlled 3D flower-like CoP<sub>3</sub>/CeO<sub>2</sub>/C heterostructures as bifunctional oxygen electrocatalysts for rechargeable Zn-air batteries, *Appl. Catal., B*, 2023, **321**, 122029.
  - 16 L. Yan, L. Cao, P. Dai, X. Gu, D. Liu, L. Li, Y. Wang and X. Zhao, Metal-organic frameworks derived nanotube of nickel-cobalt bimetal phosphides as highly efficient electrocatalysts for overall water splitting, *Adv. Funct. Mater.*, 2017, **27**, 1703455.
  - 17 Q. Chang, Y. Jin, M. Jia, Q. Yuan, C. Zhao and M. Jia, Sulfur-doped CoP@Nitrogen-doped porous carbon hollow tube as an advanced anode with excellent cycling stability for sodium-ion batteries, *J. Colloid Interface Sci.*, 2020, **575**, 61–68.
  - 18 H. Xu, J. Zhu, P. Wang, D. Chen, C. Zhang, M. Xiao, Q. Ma, H. Bai, R. Qin, J. Ma and S. Mu, Fe–Co–P multi-heterostructure arrays for efficient electrocatalytic water splitting, *J. Mater. Chem. A*, 2021, **9**, 24677–24685.
  - 19 J. Yu, Q. Li, Y. Li, C. Xu, L. Zhen, V. P. Dravid and J. Wu, Ternary metal phosphide with triple-layered structure as a low-cost and efficient electrocatalyst for bifunctional water splitting, *Adv. Funct. Mater.*, 2016, **26**, 7644–7651.
  - 20 H. Bai, D. Chen, Q. Ma, R. Qin, H. Xu, Y. Zhao, J. Chen and S. Mu, Atom Doping Engineering of Transition Metal Phosphides for Hydrogen Evolution Reactions, *Electrochem. Energy Rev.*, 2022, **5**, 24.
  - 21 H. Cao, Z. Li, Y. Xie, F. Xiao, H. Wang, X. Wang, K. Pan and A. Cabot, Hierarchical CoP nanostructures on nickel foam as efficient bifunctional catalysts for water splitting, *ChemSusChem*, 2021, **14**, 1094–1102.
  - 22 Z. Duan, H. Liu, X. Tan, A. Umar and X. Wu, Bifunctional CoP electrocatalysts for overall water splitting, *Catal. Commun.*, 2022, **162**, 106379.
  - 23 X. Huang, X. Xu, C. Li, D. Wu, D. Cheng and D. Cao, Vertical CoP nanoarray wrapped by N,P-doped carbon for hydrogen evolution reaction in both acidic and alkaline conditions, *Adv. Energy Mater.*, 2019, **9**, 1803970.
  - 24 T. Liu, P. Li, N. Yao, G. Cheng, S. Chen, W. Luo and Y. Yin, CoP-doped MOF-based electrocatalyst for pH-universal hydrogen evolution reaction, *Angew. Chem., Int. Ed.*, 2019, **58**, 4679–4684.
  - 25 H. Sun, Y. Lian, C. Yang, L. Xiong, P. Qi, Q. Mu, X. Zhao, J. Guo, Z. Deng and Y. Peng, A hierarchical nickel-carbon structure templated by metal-organic frameworks for efficient overall water splitting, *Energy Environ. Sci.*, 2018, **11**, 2363–2371.
  - 26 Y. Yin, J. Han, Y. Zhang, X. Zhang, P. Xu, Q. Yuan, L. Samad, X. Wang, Y. Wang, Z. Zhang, P. Zhang, X. Cao, B. Song and S. Jin, Contributions of phase, sulfur vacancies, and edges to the hydrogen evolution reaction catalytic activity of porous molybdenum disulfide nanosheets, *J. Am. Chem. Soc.*, 2016, **138**, 7965–7972.
  - 27 J. Feng, S. Ye, H. Xu, Y. Tong and G. Li, Design and synthesis of FeOOH/CeO<sub>2</sub> heterolayered nanotube electrocatalysts for the oxygen evolution reaction, *Adv. Mater.*, 2016, **28**, 4698–4703.
  - 28 J. Ke, J. Xiao, W. Zhu, H. Liu, R. Si, Y. Zhang and C. Yan, Dopant-induced modification of active site structure and surface bonding mode for high-performance nanocatalysts: CO oxidation on capping-free (110)-oriented CeO<sub>2</sub>:Ln (Ln = La–Lu) nanowires, *J. Am. Chem. Soc.*, 2013, **135**, 15191–15200.
  - 29 X. Long, H. Lin, D. Zhou, Y. An and S. Yang, Enhancing full water-splitting performance of transition metal bifunctional electrocatalysts in alkaline solutions by tailoring CeO<sub>2</sub>-transition metal oxides–Ni nanointerfaces, *ACS Energy Lett.*, 2018, **3**, 290–296.
  - 30 J. Chen, Z. Hu, Y. Ou, Q. Zhang, X. Qi, L. Gu and T. Liang, Interfacial engineering regulated by CeO<sub>x</sub> to boost efficiently alkaline overall water splitting and acidic hydrogen evolution reaction, *J. Mater. Sci. Technol.*, 2022, **120**, 129–138.
  - 31 W.-H. Huang, X.-M. Li, X.-F. Yang, H.-Y. Zhang, P.-B. Liu, Y.-M. Ma and X. Lu, CeO<sub>2</sub>-embedded mesoporous CoS/MoS<sub>2</sub>

- as highly efficient and robust oxygen evolution electrocatalyst, *Chem. Eng. J.*, 2021, **420**, 127595.
- 32 X. Luo, P. Ji, P. Wang, R. Cheng, D. Chen, C. Lin, J. Zhang, J. He, Z. Shi, N. Li, S. Xiao and S. Mu, Interface engineering of hierarchical branched Mo-doped Ni<sub>3</sub>S<sub>2</sub>/Ni<sub>x</sub>P<sub>y</sub> hollow heterostructure nanorods for efficient overall water splitting, *Adv. Energy Mater.*, 2020, **10**, 1903891.
- 33 J. Zhang, T. Wang, D. Pohl, B. Rellinghaus, R. Dong, S. Liu, X. Zhuang and X. Feng, Interface engineering of MoS<sub>2</sub>/Ni<sub>3</sub>S<sub>2</sub> heterostructures for highly enhanced electrochemical overall-water-splitting activity, *Angew. Chem., Int. Ed.*, 2016, **55**, 6702–6707.
- 34 P. Chen, Y. Tong, C. Wu and Y. Xie, Surface/Interfacial engineering of inorganic low-dimensional electrode materials for electrocatalysis, *Acc. Chem. Res.*, 2018, **51**, 2857–2866.
- 35 H. Huang, C. Yu, X. Han, S. Li, S. Cui, C. Zhao, H. Huang and J. Qiu, Interface engineering of Ni<sub>3</sub>N@Fe<sub>3</sub>N heterostructure supported on carbon fiber for enhanced water oxidation, *Ind. Eng. Chem. Res.*, 2017, **56**, 14245–14251.
- 36 J. Zhu and S. Mu, Parsing the basic principles to build efficient heterostructures toward electrocatalysis, *Inorg. Chem. Front.*, 2023, **10**, 2220–2225.
- 37 B. Zhang, J. Shan, W. Wang, P. Tsiakaras and Y. Li, Oxygen Vacancy and Core–Shell Heterojunction Engineering of Anemone-Like CoP@CoOOH Bifunctional Electrocatalyst for Efficient Overall Water Splitting, *Small*, 2022, **18**, 2106012.
- 38 R. Zhang, X. Ren, S. Hao, R. Ge, Z. Liu, A. M. Asiri, L. Chen, Q. Zhang and X. Sun, Selective phosphidation: an effective strategy toward CoP/CeO<sub>2</sub> interface engineering for superior alkaline hydrogen evolution electrocatalysis, *J. Mater. Chem. A*, 2018, **6**, 1985–1990.
- 39 M. Guo, M. Xu, Y. Qu, C. Hu, P. Yan, T. T. Isimjan and X. Yang, Electronic/mass transport increased hollow porous Cu<sub>3</sub>P/MoP nanospheres with strong electronic interaction for promoting oxygen reduction in Zn-air batteries, *Appl. Catal., B*, 2021, **297**, 120415.
- 40 Y. Sun, T. Liu, Z. Li, A. Meng, G. Li, L. Wang and S. Li, Morphology and interfacial charge regulation strategies constructing 3D flower-like Co@CoP<sub>2</sub> heterostructure electrocatalyst for efficient overall water splitting, *Chem. Eng. J.*, 2021, **433**, 133684.
- 41 J. Li, S. Zou, X. Liu, Y. Lu and D. Dong, Electronically Modulated CoP by Ce Doping as a Highly Efficient Electrocatalyst for Water Splitting, *ACS Sustainable Chem. Eng.*, 2020, **8**, 10009–10016.
- 42 W. Guo, H. Luo, D. Fang, Z. Jiang, J. Chi and W. Shangguan, In situ revealing the reconstruction behavior of monolayer rocksalt CoO nanosheet as water oxidation catalyst, *J. Energy Chem.*, 2022, **70**, 373–381.
- 43 B. Wang, H. Huang, T. Sun, P. Yan, T. T. Isimjan, J. Tian and X. Yang, Dissolution reconstruction of electron-transfer enhanced hierarchical NiS<sub>x</sub>-MoO<sub>2</sub> nanospheres as a promising industrialized hydrogen evolution catalyst beyond Pt/C, *J. Colloid Interface Sci.*, 2020, **567**, 339–346.
- 44 Y. Wang, X. Li, M. Zhang, J. Zhang, Z. Chen, X. Zheng, Z. Tian, N. Zhao, X. Han, K. Zaghbi, Y. Wang, Y. Deng and W. Hu, Highly Active and Durable Single-Atom Tungsten-Doped NiS<sub>0.5</sub>Se<sub>0.5</sub> Nanosheet@NiS<sub>0.5</sub>Se<sub>0.5</sub> Nanorod Heterostructures for Water Splitting, *Adv. Mater.*, 2022, **34**, 2107053.
- 45 Y. Liu, H. Zhang, W. Song, Y. Zhang, Z. Hou, G. Zhou, Z. Zhang and J. Liu, In-situ growth of ReS<sub>2</sub>/NiS heterostructure on Ni foam as an ultra-stable electrocatalyst for alkaline hydrogen generation, *Chem. Eng. J.*, 2023, **451**, 138905.
- 46 L. Wang, H. Yu, Z. Huang, Z. Luo, T. T. Isimja, S. Xu and X. Yang, Interface engineering of porous nickel-iron phosphates with enriched oxygen vacancies as an efficient bifunctional electrocatalyst for high current water splitting, *Electrochim. Acta*, 2023, **443**, 141932.
- 47 H. Ma, Z. Chen, Z. Wang, C. V. Singh and Q. Jiang, Interface Engineering of Co/CoMoN/NF Heterostructures for High-Performance Electrochemical Overall Water Splitting, *Adv. Sci.*, 2022, **9**, 2105313.
- 48 Z. Luo, Q. Peng, Z. Huang, L. Wang, Y. Yang, J. Dong, T. T. Isimjan and X. Yang, Fine-tune d-band center of cobalt vanadium oxide nanosheets by N-doping as a robust overall water splitting electrocatalyst, *J. Colloid Interface Sci.*, 2023, **629**, 111–120.
- 49 D. Bhutani, S. Maity, S. Chaturvedi, D. Chalapathi, U. V. Waghmare, C. Narayana, V. C. Prabhakaran and E. Muthusamy, Heterostructure from heteromixture: unusual OER activity of FeP and CoP nanostructures on physical mixing, *J. Mater. Chem. A*, 2022, **10**, 22354–22362.
- 50 B. Wang, H. Huang, M. Huang, P. Yan, T. T. Isimjan and X. Yang, Electron-transfer enhanced MoO<sub>2</sub>-Ni heterostructures as a highly efficient pH-universal catalyst for hydrogen evolution, *Sci. China: Chem.*, 2020, **63**, 841–849.
- 51 Y.-P. Zhu, X. Xu, H. Su, Y.-P. Liu, T. Chen and Z.-Y. Yuan, Ultrafine Metal Phosphide Nanocrystals in Situ Decorated on Highly Porous Heteroatom-Doped Carbons for Active Electrocatalytic Hydrogen Evolution, *ACS Appl. Mater. Interfaces*, 2015, **7**, 28369–28376.
- 52 Y. Wu, Y. Zhao, P. Zhai, C. Wang, J. Gao, L. Sun and J. Hou, Triggering Lattice Oxygen Activation of Single-Atomic Mo Sites Anchored on Ni-Fe Oxyhydroxides Nanoarrays for Electrochemical Water Oxidation, *Adv. Mater.*, 2022, **34**, 2202523.
- 53 T. Jia, J. Wu, Y. Xiao, Q. Liu, Q. Wu, Y. Qi and X. Qi, Self-grown oxygen vacancies-rich CeO<sub>2</sub>/BiOBr Z-scheme heterojunction decorated with rGO as charge transfer channel for enhanced photocatalytic oxidation of elemental mercury, *J. Colloid Interface Sci.*, 2021, **587**, 402–416.
- 54 C. Wu, J. Guo, J. Zhang, Y. Zhao, J. Tian, T. T. Isimjan and X. Yang, Palladium nanoclusters decorated partially decomposed porous ZIF-67 polyhedron with ultrahigh catalytic activity and stability on hydrogen generation, *Renewable Energy*, 2019, **136**, 1064–1070.
- 55 W. Chen, X. Zhu, R. Wang, W. Wei, M. Liu, S. Dong, K. K. Ostrikov and S.-Q. Zang, Interface-engineered MoS<sub>2</sub>/CoS/NF bifunctional catalysts for highly-efficient water electrolysis, *J. Energy Chem.*, 2022, **75**, 16–25.
- 56 Y. Huang, X. Hu, J. Li, J. Zhang, D. Cai, B. Sa, H. Zhan and Z. Wen, Rational construction of heterostructured core-shell

- Bi<sub>2</sub>S<sub>3</sub>@Co<sub>9</sub>S<sub>8</sub> complex hollow particles toward high-performance Li- and Na-ion storage, *Energy Storage Mater.*, 2020, **29**, 121–130.
- 57 X. Li, Y. Wang, J. Wang, Y. Da, J. Zhang, L. Li, C. Zhong, Y. Deng, X. Han and W. Hu, Sequential Electrodeposition of Bifunctional Catalytically Active Structures in MoO<sub>3</sub>/Ni–NiO Composite Electrocatalysts for Selective Hydrogen and Oxygen Evolution, *Adv. Mater.*, 2020, **32**, 2003414.
- 58 J. Lin, P. Wang, H. Wang, C. Li, X. Si, J. Qi, J. Cao, Z. Zhong, W. Fei and J. Feng, Defect-Rich Heterogeneous MoS<sub>2</sub>/NiS<sub>2</sub> Nanosheets Electrocatalysts for Efficient Overall Water Splitting, *Adv. Sci.*, 2019, **6**, 1900246.